Article

Synthesis-structure-activity relations in Fe-CHA for C-H activation: control of Al-distribution by interzeolite conversion

Julien Devos, Max L. Bols, Dieter Plessers, Cédric Van Goethem, Jin Won Seo, Son-Jong Hwang, Bert F. Sels, and Michiel Dusselier

Chem. Mater., **Just Accepted Manuscript** • DOI: 10.1021/acs.chemmater.9b03738 • Publication Date (Web): 27 Nov 2019

Synthesis-structure-activity relations in Fe-CHA for C-H activation: control of Al-distribution by interzeolite conversion

Julien Devos,† Max L. Bols,† Dieter Plessers,† Cédric Van Goethem‡, Jin Won Seo^, Son-Jong Hwang°, Bert F. Sels† and Michiel Dusselier†,*

† Center for Sustainable Catalysis and Engineering (CSCE), KU Leuven, Celestijnenlaan 200F, B-3001 Leuven, Belgium.

‡ Centre for Membrane Separations, Adsorption, Catalysis and Spectroscopy for Sustainable Solutions (cMACS), Celestijnenlaan 200F, B-3001 Leuven, Belgium.

^ Department of Materials Engineering (MTM), KU Leuven, Kasteelpark Arenberg 44 – bus 2450, B-3001 Leuven, Belgium.

° Division of Chemistry and Chemical Engineering, California Institute of Technology, Pasadena, California 91125, USA.

Supporting Information Placeholder

ABSTRACT: The search for structurally relevant Al-arrangements in zeolites is an important endeavor for single site catalysis. Little is known about the mechanisms and zeolite dynamics during synthesis that are responsible for creating those Al-ensembles. Here, new synthetic strategies for creating Al-hosts in small-pore zeolites suitable for divalent cation catalysis are uncovered, leading to a mechanistic proposal for Al-organization during crystallization. As such, unique synthesis-structure-activity relations are demonstrated for the partial oxidation of methane on Fe-exchanged CHA-zeolites. With modified interzeolite conversions, the divalent cation capacity of the resulting high Si SSZ-13 zeolites (Si/Al ~ 35) can be reproducibly controlled in a range between 0.04 and 0.34 Co^{2+}/Al. This capacity is a proxy for the distribution of framework aluminum in pairs and correlates with the methanol production per Al when these zeolites host the α-Fe^{II} redox active site. The uncovered IZC synthesis-structure relations paint an Al-distribution hypothesis, where incongruent dissolution of the starting USY zeolite and fast synthesis kinetics with atypical growth modes allow assembling specific Al-arrangements, resulting in a high divalent cation capacity. Prolonged synthesis times and high temperatures overcome the energetic barriers for T-atom reshuffling favoring Al-isolation. These mechanisms and the relations uncovered in this work will guide the search for relevant Al-ensembles in a range of zeolite catalysts where controlling the environment for a single active site is crucial.

1. INTRODUCTION

The use of small-pore zeolites,[1-2] with channels bounded by rings of at most eight tetrahedra, is gaining traction as evidenced by their recent industrial implementation of methanol-to-olefins (MTO)[3-5] and selective catalytic reduction (SCR: NOx abatement) processes.[6-9] A key challenge in gas-phase catalysis is the C-H activation of methane by direct partial oxidation to methanol.[10-12] This redox process is possible with reactive oxygen species (ROS) formed on transition metal ion- (TMI-) exchanged zeolites and was originally demonstrated on medium and large pore topologies.[13] Methane partial oxidation on small-pore zeolites was only recently demonstrated, using Cu cations in SSZ-13 (CHA) and SSZ-39 (AEI) by Lobo and co-workers.[14-16] Multiple active Cu species have been proposed.[17-22] Finding a straightforward relation between Cu active sites and the Al arrangement of the zeolite host is difficult,[7, 23] let alone controlling that arrangement. The dynamic nature of Cu[24-25] and the presumed mono, di- or multinuclear active sites does not help.[13,17-21]

Besides the Cu-systems, which can form the ROS using O_2, ROS capable of methane activation even at room temperature can also be formed on iron-exchanged zeolites with the α-Fe^{II} precursor using N_2O as oxidant.[26] Recently, Bols et al. reported the first small-pore iron-containing zeolite (Fe-SSZ-13) with decent activity and a well-defined active site. The active site is identified as a mononuclear isolated extraframework Fe^{II} species stabilized by 6-membered ring (6MR) containing two opposite tetrahedral Al atoms, and this configuration was found to be thermodynamically preferred.[27] Moreover, the near exclusive presence of only the active α-Fe^{II} species was noted at low iron loadings using Mössbauer spectroscopy while at higher loadings, other undesired iron species (spectators) are formed.[26, 28] As a consequence, further improvement in the productivity in MPO will benefit from control over the Al-distribution of the host zeolite (Scheme 1).

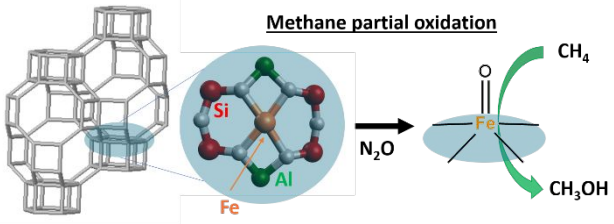

Scheme 1. Importance of Al location for methane partial oxidation (MPO) in Fe,H-SSZ-13 (CHA framework on left) using N_2O as oxidant. Green: Al, red: Si, grey: framework O, orange: α-Fe^{II}.

Zeolite synthesis and the resulting Al distribution depend on a complex interplay between Al and Si precursors, mineralizing agent (OH^-) and stabilizing (in)organic structure directing agents (OSDA). Atomic Al-distribution can be considered a result of kinetics[29-30], however in some cases specific electronic stabilization effects could play a decisive role.[31-36] In the latter cases, the structure directing agents are presumed to influence the position of Al at the atomic length scale in the resulting zeolite. Techniques for the quantification of relevant Al configurations are not straightforward.[37-38] Only recently, synthetic control over Al distribution with implications for catalysis has been reported, mostly for larger pore zeolites.[32-33, 39-41]

Dědeček et al. reported a practical Co^{2+} titration method to probe proximate Al arrangements, i.e. two tetrahedral Al close enough to exchange divalent cations.[38, 42] Such probe method is particularly interesting since it includes effects of site accessibility from the aqueous ion-exchange. However, unambiguously relating the exchange of cobalt species to specific Al-arrangements remains a difficult task, especially in zeolites with variable properties such as Si/Al, defect sites and of course the variety of possible T-site combinations (2Al), even for topologies with one crystallographic T-atom position (e.g. as in CHA).[43] Computational studies demonstrate the presence of 25 symmetry-distinct combinations within the CHA unit cell containing two Al atoms (Si/Al=17) and 210 possible combinations to counterbalance a divalent cation on these 25 configurations, due to the four possible acidic O_F (framework oxygen) neighboring each Al.[44] The most stable combination, at least in certain conditions, is often found to be a divalent cation in square planar coordination on two opposite Al tetrahedra in a 6MR in SSZ-13 materials (Cu^{2+},[45] Co^{2+} [43] and Fe^{2+} [27-28]).

Di Iorio and Gounder pioneered synthetic control over the Al-distribution in SSZ-13 in the context of acid-catalyzed reactions (methanol to dimethylether).[34, 37, 40] A maximal content of Al in pairs in SSZ-13, defined there as 2 Al in a 6MR, opposite or not, and probed by Co^{2+}-exchanged capacity, was achieved from batch compositions containing an equimolar presence of N,N,N-Trimethyl-1-Adamantammonium hydroxide ($TMAda^+$) and Na^+ for systems with Si/Al ratios of 15-25. In their specific synthesis the maximal Al pairing coincided with the Al pairing expected for randomized distribution of Al in pairs at a specific Si/Al ratio (e.g. Co^{2+}/Al = 0.08 for Si/Al= 15),[34] with a maximum of 44% Al in pairs reported (Co^{2+}/Al = 0.22).[40] Whereas the direct relation between pairs (2 Al in a 6MR) and Co^{2+}-exchange is hard to prove within CHA-zeolites,[43] the Co^{2+}/Al ratio can be used as measure for the divalent cation capacity (DCC) of a zeolite.

In this work we report FAU-to-CHA interzeolite conversion (IZC) syntheses with control over a broad range of DCC, i.e. Co^{2+}/Al, from 0.04 to 0.34, for high silica CHA-zeolites with comparable Al content. Next, we show that the DCC allows to predict the activity, in terms of methanol production per Al, if these zeolites are used as hosts for the Fe^{II} active site for methane to methanol partial oxidation. For the first time with redox zeolites, it is demonstrated that specific syntheses with high DCC allow a higher (MPO) activity than expected from a randomized Al distribution, showcasing the effectiveness of synthesis strategies. The uncovered synthesis-structure relations support an Al-distribution hypothesis for IZC, where a fast synthesis rate and the creation of Al dense regions favor elevated DCC, while prolonged synthesis times and thermodynamic contributions seem to service the isolation of Al. A case-specific investigation of structural properties during the FAU-to-CHA evolution provides more insight on the fate of Al during the crystallization period. This leads to a substantiated mechanistic proposal for Al organization during crystallization (from IZC) with potential implications for numerous other zeolites and synthesis methods.

2. EXPERIMENTAL SECTION

2.1. Zeolite preparation and characterization

2.1.1. CHA (SSZ-13) Synthesis. All high silica SSZ-13 zeolites were prepared with strict control over reactants and synthesis conditions. For IZC syntheses the starting materials are FAU-type zeolites (CBV780, zeolyst). For amorphous source syntheses LUDOX HS-40 (40wt.% SiO_2, Sigma-Aldrich) was used as Si source and aluminum hydroxide (Al_2O_3, >66%, Sigma-Aldrich) as Al-source. In all syntheses N,N,N-Trimethyl-1-Adamantammonium hydroxide (TMAdaOH, Sachem) is used as OSDA possibly with additional deionized water (18.2 MΩ). The solution was added directly in a 23ml Teflon liner reactor, followed by internal stirring (PTFE stirring bar, 20x6mm) and introduction of the source materials, the Si-source prior to the Al source in the case of amorphous sources. The complete mixtures were internally stirred until a homogenous mixture was obtained (~1min. for IZC syntheses, 5min. for Am* syntheses). Next, the Teflon liners were brought in the corresponding stainless steel autoclaves (Acid digestion vessel 4749, Parr instruments) and heated in a forced convection oven (Heratherm, ThermoSientific) under 600rpm internal stirring (heat resistant multi-position stirring plate, 2mag) at the corresponding synthesis temperature. After synthesis, the reactors were cooled and the solids were recovered by centrifugation (6000rpm, ≥5min) and washed at least 3 times (±50mL solvent per g solids) with deionized water (18.2 MΩ) until the supernatant shows pH below 9. After a final washing step with acetone the solids were oven-dried overnight at 100°C, yielding the as-synthesized materials. The OSDA in the zeolite pores was removed by calcination in air at 580°C for 6h after ramping the furnace at 1°C/min from ambient conditions (LV9/11, Nabertherm).

2.1.2. Cobalt cation exchange. The divalent cation capacity (DCC) was determined by aqueous Co-exchange and ICP-AES, closely similar to the method of Dědeček et al.[38] under ambient conditions to probe specific atomic configurations (proximate Al). This method, adapted by multiple authors[41, 46-48] studying Al distributions, uses a 0.05M $Co(NO_3)_2$ solution, starting from Na-SSZ-13.

First, H^+-(or partial Na^+/H^+)-SSZ-13 were converted to the Na^+-form via aqueous phase ion-exchange using 150 ml of an aqueous 0.5 M NaCl (>99% ,VWR) solution per g solids at ambient conditions under stirring. This procedure is repeated 3 times with respectively 16 hour, 8 hour and 16 hour exchange times. After exchange the solids were separated by centrifugation and washed at least three times with millipore water (>150 ml per g solids). Subsequently, Na^+-form SSZ-13 is oven-dried at 373 K.

The Co exchange procedure is similar to Na-SSZ-13 exchange, using 150 ml of an aqueous 0.05 M $Co(NO_3)_2$ (>99%, Acros Organics) solution per g Na-exchanged SSZ-13 at ambient conditions under stirring. This procedure is repeated 3 times with respectively 16 hour, 8 hour and 16 hour exchange times. After exchange the solids are separated by centrifugation and washed at least three times with millipore water (>150 ml per g solids). (Co,Na)-form zeolites are oven-dried at 373 K overnight.

2.1.3. Characterization. The structure and crystallinity of the zeolites were confirmed by X-ray powder diffraction (PXRD) on a high-throughput STOE STADI P Combi diffractometer in transmission mode with focusing Ge(111) monochromatic X-ray inlet beams (λ = 1.5406 Å, Cu Kα source).

Porosity is measured by nitrogen physisorption (Tristar II 3020, micrometrics) at 77 K on calcined and dried samples (6 h at 300 °C). The relative nitrogen pressure is varied between 0.01 and 0.99 (p/p_0). The *t*-plot method (Harkins and Jura) on the adsorption branch is used to determine micropore volumes.

The elemental analysis was performed using an inductively coupled plasma-atomic emission spectrometer (ICP-AES, Perkin Elmer Optima 3300 DV) with signal for Co, Fe, Al and Si at 308.2, 228.6, 238.2 and 251.6nm respectively. Before ICP-AES, the samples were dissolved using HF and aqua regia, neutralized using boric acid and diluted using 0.42 M HNO_3 in water.

Thermogravimetric analysis (TGA) for as-synthesized SSZ-13 was performed on a TA Instruments TGA Q500. The relative content of occluded $TMAda^+$ was measured between as weight loss between 473K and 973K using O_2 flow.

TEM-samples were prepared by drop-casting a dispersion of the particles on a holey carbon-coated TEM grid (Cu, 300 mesh, Pacific Grid Tech Ltd.). TEM was performed using a JEOL ARM200F microscope operated at 200kV and equipped with a

cold FEG and a probe aberration corrector. EDX analysis of the samples was performed using a Centurio EDX detector with a large solid angle of 0.98 steradians from a 100mm² detection area. ^{27}Al and ^{29}Si solid state nuclear magnetic resonance (SS NMR) were measured on a Bruker 500 MHz NMR spectrometer and using a Bruker 4 mm MAS probe. ^{29}Si MAS NMR was recorded after 4-µs 90 degree pulse under a sample spinning rate of 8 kHz and referenced to externally tetramethylsilane (TMS). Solid-state ^{27}Al MAS NMR was measured at spinning rate of 13 kHz and referenced to 1 M aq. aluminum nitrate.

2.2. Sample Treatment for Methane Partial Oxidation (MPO)

2.2.1. Introduction of Fe in SSZ-13. Fe,H-SSZ-13 materials were prepared according to the strategy used by Bols and co-workers.[26-27] Iron was introduced into dried H-CHA by diffusion impregnation in a solution of $Fe(acac)_3$ in toluene (25 mL/g zeolite) for 24h. The concentration of $Fe(acac)_3$ in toluene is approximately 7.6 mM. All samples were washed thoroughly in toluene and oven-calcined in air with a heating ramp of 2 °C/min to 550 °C for 30 h (LV9/11, Nabertherm).

2.2.2. Methane partial activation procedure. Calcined Fe-CHA samples were loaded in a quartz reactor fitted with a window for DR-UV−Vis−NIR measurements. A standard treatment procedure consists of an activation step in a 20 mL/min flow of dried He with a heating ramp of 10°C/min to the end temperature of 900°C which is maintained for 2 h, a 20 min treatment in a 35% N_2O/He atmosphere at 180 °C, and a 30 min treatment in 30 mL/min CH_4 flow at room temperature. All flows were controlled with mass flow controllers (Brooks Instrument 0154). Flows are given for STP conditions.

2.2.3. MeOH batch extraction. A known mass (~0.2 g) of dry sample was transferred into a 7 mL screw lid vial with 1 mL of distilled water, 1 mL of acetonitrile and a stirring rod. The mixture was allowed to stir for 24 h (800 rpm) at room temperature and then centrifuged. The solution was analyzed on an Agilent 6850 gas chromatograph fitted with an HP1 column and a flame ionization detector (GC-FID).

2.3. Synthesis evolution tests

SSZ-13 recipes are made in standard batch conditions (1Si: 0.025Al: 0.35$TMAda^+$: 0.35OH^-: 12.5H_2O) using 2.6g of CBV780 (US-Y, zeolyst) and according to standard procedures (cfr. 2.1.1.). Batches are taken out of the synthesis oven at regular time intervals, water-bath cooled for 15min and transferred for centrifugation (15 minutes at 6700rpm, 7177g). Next, the liquid fraction is carefully decanted, while the solid fraction is subsequently washed two times with 20ml Millipore water and oven-dried overnight (100°C). Solid yields are determined after overnight drying, and the samples are subjected to thermogravimetric (TGA) analysis under the same atmospheric conditions (preventing uncontrolled water sorption). The chemical composition of the solid products is determined by combination of element analysis (ICP-AES) and TGA (only ICP-AES for liquid). Remaining weight in TGA after a cycle between room temperature and 800°C is used to determine the pure zeolitic fraction (TO_2-atoms). Other measured weights/fractions are tabulated (Table S5).

3. RESULS AND ANALYSIS

3.1. Difference in synthesis-structure-activity of SSZ-13 from different T-atom sources

3.1.1. Synthesis of SSZ-13 from different sources. Stoichiometrically identical synthesis batches with differing Si and Al sources are used in SSZ-13 synthesis under identical conditions to demonstrate the effect of the T-atom sources on DCC (2.1.2., Experimental Section). The use of inorganic (alkali) cations is omitted to eliminate their contribution to structure and Al-direction.[34, 40] The batch composition 1SiO_2: 0.025Al: 0.35$TMAda^+$: 0.35OH^-: 18H_2O was obtained using colloidal silica and aluminum hydroxide as Si and Al source respectively, on one hand, and using a zeolite on the other. The latter procedure relies on using USY zeolites with a Si/Al ratio of 40 and is also known as interzeolite conversion (IZC). These latter syntheses provide the advantage of FAU being readily available with high synthetic purity.[49] In total three replications were made for each synthesis type. All six syntheses resulted in phase-pure SSZ-13 (CHA) with very similar physical properties (Table S1). The samples shows consistently high crystallinity (PXRD, Figure S1), identical micropore volumes (Table S1, Figure S2) and identical OSDA-to-cage ratios (ca. 1) as determined from TGA (Table S2, Figure S3). SS NMR spectra prove the sole presence of tetrahedrally coordinated Si and Al (Figure S4) in the calcined materials.

3.1.2. Divalent cation capacity (DCC) of SSZ-13 from different sources. The calcined zeolites were compared in terms of divalent cation capacity (DCC), defined here by the Co^{2+}/Al ratio, after repeated aqueous ion-exchange at room temperature. Table 1 summarizes the relevant characterization on exchanged SSZ-13 zeolites made using amorphous sources (colloidal silica and $Al(OH)_3$) or via IZC, respectively. In line with previous findings for amorphous or soluble synthesis sources using only OSDA without Na^+, the separate T-atom precursors lead to full Al-isolation and virtually no DCC (Co/Al=0.005). The IZC zeolites however show high DCC values, i.e. Co/Al= 0.24 (± 0.02) (Table 1). These values are unusually high for SSZ-13 (Si/Al > 25).[34] Compared to literature of Co^{2+} exchange on SSZ-13 with more Al (Si/Al < 15), these Co/Al values are not uncommon.[40, 43]A strikingly large difference in DCC is thus observed for synthesized SSZ-13s with seemingly similar physico-chemical properties (Section S.1., Supporting Information). Assuming the local Al organization is probed within zeolitic cages (credible assumption discussed in Section S.2., Supporting Information), it can be concluded that a different Al distribution dynamic seems at play in IZC *versus* the conventional syntheses using amorphous sources. This corroborates the observations of Nishitoba et al. on the diversity of Al distribution observed in SSZ-13 made from FAU and amorphous materials.[50] Using SS NMR they attributed more AlOSiOAl (next-nearest-neighbor) arrangements in SSZ-13 made from IZC. Their synthesis systems are however much more aluminous (Si/Al_F=15) which intrinsically favors high DCC. Our results (section 3.1) are the first to demonstrate that Na^+ is not required to yield high DCC in SSZ-13 materials, suggesting that during crystallization solely $TMAda^+$ is capable of directing *proximate Al* formation, i.e. two spatially close Al T-atoms within the same *cha*-cage. Theoretically, an overall Si/Al_F=~35 only translates to 1 Al in each geometric *cha*-cage (a net of 36 T-atoms), shared over 3 neighboring *cha* cages (Figure S5).[1] These first results indicate that the IZC synthetic approach is a good candidate to crystallize SSZ-13 with high hosting capacities for divalent cations (DCC). Such zeolites may allow a high density of active sites (and their host ensembles) for redox catalysis.

Table 1. Si/Al, divalent cation capacity (DCC), Fe-uptake and methanol productivity for two SSZ-13 zeolites synthesized from identical batch compositions but different sources.

Sources	**Si/Al**	**DCC** (Co/Al)	**Fe-uptake** (Fe/Al)	MeOH prod. [a] (µmol/g zeo.)
Colloïdal silica+ $Al(OH)_3$ (Am*)	28 (±3) [b]	0.005 (±0.003) [b]	0.06 [c]	1.5 [c]
US-Y zeolite (IZC)	37 (±2) [b]	0.24 (±0.02) [b]	0.17 [d]	36 [d]

[a]MeOH productivity from methane partial oxidation (MPO)
[b] average of 3 (synthesis + ion exchange) replications, DCC of

individual samples given in Table S1; [c] based on sample Am*-3; MeOH value close to lower detection limit; [d] based on IZC-2.

3.1.3. Methane partial oxidation on SSZ-13 from different sources. Bols et al. hinted to the importance of Al-distribution for methane partial oxidation (MPO) on Fe-exchanged SSZ-13 materials.[27] A sample of each synthesis type (amorphous sources Am*-3 vs. IZC-2) was subjected to an identical MPO procedure. Although both samples are open SSZ-13 zeolites with similar physico-chemical properties, they take up iron to a different extent: Am*-3 exchanges 0.06 Fe/Al, compared to 0.17 Fe/Al for IZC-2. This indicates DCC to be a decent descriptor for multivalent Fe-exchange. STEM-EDX showed a homogenous distribution of Si, Al, and O by elemental mapping over a single crystal, and also that Fe can exchange through the full interior of the crystal (Figure S9). Besides homogeneous Fe, mapping of Fe as well as TEM (bright field) revealed the presence of a small fraction of aggregated dense Fe clusters on the surface (Figure S9-S10).

Following MPO with one activation cycle, no significant amount of MeOH was extracted from the sample with very low DCC (0.3 µmol/g zeolite), whereas 36 µmol/g was extracted from the IZC zeolite with high DCC (Table 1). DR-UV-Vis-NIR spectra (Figure S11) of SSZ-13 with high DCC proved the formation of the typical α-Fe and α-O absorption bands of the active site (Scheme 1), while such bands are absent in samples with very low DCC (Section S.3.1, Supporting Information). These results align with our earlier observations by ^{57}Fe Mössbauer and electronic spectroscopy, that assigned divalent α-Fe^{II} species – located in 6MRs where two Al atoms are sited opposite of each other – as the active species for MPO in Fe-SSZ-13.[27] The link between MeOH productivity and DCC strengthens these findings and further suggests DCC as a descriptor for Al arrangements that allow Fe based MPO. In contrast, Fe exchange and MeOH productivity showed much less correlation: Am*-3 does incorporate a minor portion of Fe (Fe/Al=0.06) but is not active for MPO, while IZC-2 also incorporates some likely inactive oxide clusters (Figure S9-S10). During Fe-exchange, the tendency for oxide formation is higher than during Co exchange, qualifying the latter as the superior divalent probe.[51] In what follows, the DCC method will be used to probe synthesis-structure relations for SSZ-13 zeolites made in a range of IZC conditions (3.2), simultaneously functioning as an indicator for the suitability to host α-Fe^{II} sites for MPO (3.3).

3.2. Synthesis-DCC relations in SSZ-13 zeolites from IZC

The striking divergence of DCC values for similar compositions, and the high DCC for a Si/Al = 37 zeolite via IZC, prompted a single-parameter study to understand DCC generation in the FAU-to-CHA system. IZC series were made using different batch compositions and multiple reproductions (Table S4), relying on specific molar batch compositions: $1SiO_2$: 0.025Al: x$TMAda^+$: xOH^-: yH_2O with x = [0.10 - 0.67] and y = [5 - 100], as well as variations in synthesis temperature and time. As a benchmark, seven reproductions were made of a 'standard' synthesis recipe of $1SiO_2$: 0.025Al: 0.35$TMAda^+$: 0.35OH^-: 12.5H_2O at 160°C under stirring (600rpm). These zeolites have similar physico-chemical properties (Table S4-series I) and DCC (Co/Al= 0.23 (± 0.01)) demonstrating reproducibility despite the many consecutive experimental steps.

3.2.1. TMAda-OH content. Variation of organic content has the largest impact on SSZ-13 synthesis. Both the $TMAda^+$ and OH^- ions have a crucial role in SSZ-13 crystallization, as OSDA and as mineralizing agent respectively.[29] In total, 17 zeolites (including reproductions) were made using molar batch compositions: $1SiO_2$: 0.025Al: x$TMAda^+$: xOH^-: 12.5H_2O with x = [0.10 - 0.67]. Open and pure CHA zeolites are obtained in a broad synthesis range ($TMAda^+$/Si=[0.10 - 0.45]). All these SSZ-13 materials have comparable bulk properties: crystallinity, Si/Al_F and micropore volume (Table S4-series II). Despite variation of $TMAda^+$ content in the starting composition, similar organic contents are found occluded after synthesis (Table S2, ca. 1 OSDA per cage). The lower boundary for achieving pure SSZ-13 crystallization ($TMAda^+$/Si = 0.1) does not exceed the quantity needed for filling all cages with one organic by a lot (= $TMAda^+$/Si ≈ 0.08). Syntheses from $TMAda^+$/Si ratio's in excess of 0.45 start to become phase-impure as evidenced by additional reflections in PXRD resembling those of a layered phase (Figure S12). Irrespective of the low variability of most bulk parameters, a significant variation in DCC and thus Al-distribution can be observed as a function of the OSDA (and concomitant OH^-) content of a synthesis (Figure 1A). In the low concentration region, a very low DCC is found, while high OSDA-OH concentrations tend to yield higher DCC's, with a maximum of ~0.24 Co/Al for zeolites made with TMAdaOH/Si=0.35. Further augmentation lowers DCC, and eventually CHA phase selectivity.

3.2.2. Water content. Figure 1B shows the effect of synthesis dilution on DCC. Again, over a broad range of conditions (H_2O/Si=[5 -100]) pure and open SSZ-13 is observed with very few differences in bulk properties (Table S4-series III). Generally, more concentrated mixtures (low H_2O/Si) tend to form SSZ-13 with higher Co^{2+} uptake (DCC) than samples prepared from more diluted media. The effect of dilution on DCC is less pronounced than TMAdaOH variations. In media with variable dilution the ratios among interacting species ($TMAda^+$/Si) remains the same. To deconvolute such effects, a dilution series with constant OH^-/H_2O but increasing $TMAda^+$/Si, and therefore also increasing H_2O/Si, was analyzed (Figure S14). These experiments demonstrated behavior similar to the $TMAda^+$/Si trend inferring that the ratios of $TMAda^+$ and OH^- to Si (and Al) are more important for the SSZ-13 outcome in terms of DCC than merely the contribution of $TMAda^+$ and hydroxide concentration (Section S.4.1., Supporting Information).

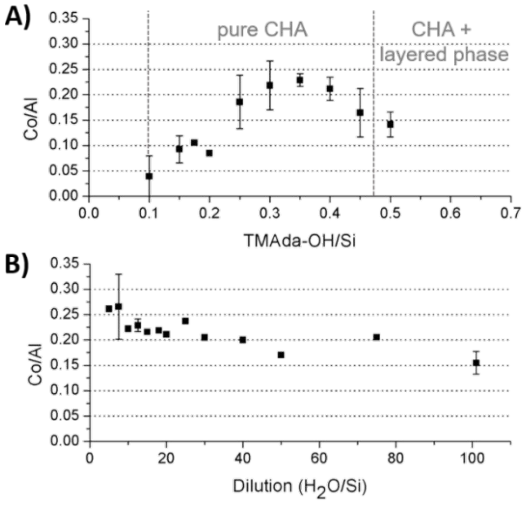

Figure 1. Effect of single parameter variations in SSZ-13 synthesis on DCC (molar Co/Al). A) Variation of OSDA concentration versus Si: [$1SiO_2$:0.025 Al: x $TMAda^+$: x OH^-:12.5 H_2O with x= [0.10 - 0.67]. B) Variation in dilution (H_2O/Si): [$1SiO_2$: 0.025Al: 0.35 $TMAda^+$:0.35 OH^-:y H_2O with y = [5 - 100]]. All zeolites were made with USY Si/Al = 40, water and aq. OSDA as starting reagents. Synthesis conditions: 160°C, 4 days, 600 rpm. One standard deviation is indicated, based on 2 to 7 repeat experiments, see Table S4.

3.2.3. Synthesis time. Hydrothermal FAU-to-CHA crystallization under standard conditions ($1SiO_2$: 0.025Al: 0.35 $TMAda^+$: 0.35 OH^-: 12.5 H_2O and 160°C, no Na^+) was followed at different times. Surprisingly the synthesis medium requires less than 3h to form an SSZ-13 phase. Although the yield seems to gradually increase with time, from 57% (3h) to 89% (18d), all these materials show similar PXRD features, crystallinity, microporosity and cage-filling (Table S4-series IV). TEM imaging revealed no clear differences in crystal sizes between calcined samples of SSZ-13 made in 6 hours, 4 or 16 days (Figure S13), with regular, cubic 150 nm crystals dominating. Surprisingly, Co-probing along the time series revealed that the highest DCC, *viz*. Co/Al is 0.31, is found in freshly formed SSZ-13 (3 hours synthesis), and continuously drops with prolonged synthesis times (or time in the medium). A 50% decline in Co/Al is observed before the Co/Al stabilizes after 12 days (Figure 2A).

3.2.4. Synthesis temperature. High Si FAU-to-CHA IZC is possible in a broad range of temperatures. Pure phase SSZ-13 is obtained by hydrothermal synthesis from 100°C to 175°C within four days under standard composition with good yields (Table S4-Series V). Higher temperatures (≥160°C) are detrimental for a high DCC in 4 day syntheses (Figure 2B). The temperature series was also conducted for 6h and 1 day synthesis. Interestingly, DCC of SSZ-13 synthesized at 175°C drops more severely with prolonged synthesis times than at 160°C. A 12 day synthesis at 180 °C yielded a DCC of only Co/Al=0.07, confirming that both prolonged exposure and high temperatures indeed favor lower DCCs (Table S4, Temp.-15). A series of IZC experiments at lower temperatures (<160°C) demonstrates the potential to maximize the DCC of SSZ-13 further. Synthesis times of 6 hours are insufficient to yield SSZ-13 at temperatures below 140 °C, and likewise, one day is not enough to form SSZ-13 at 100 °C. One day syntheses seem to produce an optimum for DCC at 140 °C (Co/Al = 0.34), while 4 day syntheses reach their maximum at 120 °C. A non-monotonic trend (vs. 160 °C in Fig. 2A) is observed at 120°C and 140°C

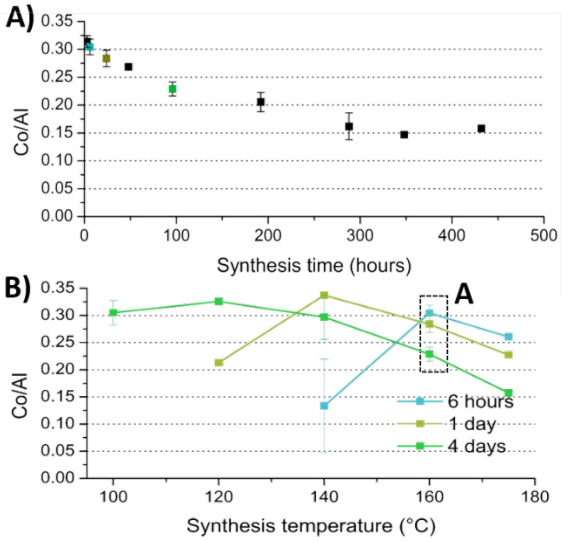

Figure 2. Effect of single parameter variations in SSZ-13 synthesis on DCC (Co/Al). A) Variation of synthesis time at 160 °C and B) Variation of synthesis temperatures and time. Controlled synthesis conditions were $1SiO_2$: 0.025 Al:0.35 $TMAda^+$:0.35 OH^-:12.5 H_2O; all zeolites were made with USY Si/Al = 40, water and aq. OSDA as starting reagents at 600 rpm. One standard deviation is indicated, based on 2 to 7 repeat experiments, see Table S4.

3.2.5. Synthesis from other crystalline sources. High Si MFI-to-CHA IZC has been performed under identical standard conditions using ZSM-5 (CBV 8014, Si/Al 40, Zeolyst) as source instead of FAU. After 19 hours of synthesis, a highly crystalline SSZ-13 (MFI-1, Table S4) has been recovered. As such, the conditions used in this work are also favoring SSZ-13 formation from MFI, so far not reported to the best of our knowledge. Interestingly, a more dense zeolite (framework density, FD_{MFI} = 18.4) is transformed into a more open one (FD_{CHA} = 15.1). Dense to more open IZCs are rare: LTL-to-CHA is known[52] and recently MFI-to-AEI was reported.[53] The DCC of our resulting SSZ-13 was significantly lower (Co/Al = 0.06) than compared to one made from FAU (Co/Al = 0.28 in 24h, Table S2: Series IV). Although not in the scope here, this is interesting for further study, because the MFI source can be hypothesized to be more stable (towards dissolution) under our conditions vs. a steamed, mesoporous, defect-rich FAU. The role of zeolite pre-treatment in their degradation processes in alkaline media was e.g. reported by Cizmek et al.[54]

3.2.6. Analysis of Synthetic factors contributing to DCC variation. Assuming a reliable link between DCC and internal Al-organization,[34, 40, 42] we can now analyze how the investigated parameters in the FAU-to-CHA (Na^+-free) crystallization space affect the Al distribution in SSZ-13 and engineer formulations to tune these distributions for specific catalytic applications. Within the broad FAU-to-CHA synthesis space, high-Si SSZ-13 with high DCCs are obtained with intermediate OSDA-to-Si ratios (3.2.1), low water content (3.2.2), relatively short synthesis times (3.2.3) and intermediate temperatures (3.2.4).

The results of the OSDA trend (Figure 1A) indicate that the most favorable conditions for high DCC are related to fast synthesis kinetics, indicating that OH/Si=0.35 represents excellent conditions for swift SSZ-13 crystallization. Likely, the dilution effect is also related to this trend as a higher pH in more dense syntheses (low H_2O to Si) also stimulates kinetics.[29] Synthesis from different zeolitic sources also indicates a severe kinetic influence on the DCC in SSZ-13, given differences in solubility of the (pre-treated) source zeolites (3.2.5).[54] The mechanisms behind the non-monotonic trend for DCC evolution in time at 120°C and 140°C remain unclear. Potentially, non-tetrahedral Al is initially incorporated at low synthesis temperatures, as noted recently for ZSM-5.[55] The DCC lowering observed for prolonged synthesis duration at higher temperatures (≥160°C; ≥3h) reflects a different cause. The augmenting solid yields and slightly increasing Si/Al product ratios at prolonged times (Figure S15) are not sufficient to explain the 50% drop in DCC, even if in specific conditions later assembled SSZ-13 would be assumed to bring no DCC (Section S4.2., Supporting Information for detailed calculations). TEM results (Figure S13) also exclude further growth of the early formed crystals (6 hours) to much larger dimensions at 4 days and even 12 days of synthesis, despite the DCC dropping from Co/Al= 0.31 (6h) to 0.14 (12 days) in these samples. The processes that cause a drop in DCC in time seems to involve the passage over a high energetic barrier *en route* to a thermodynamically favored lower energy state. Since zeolite compositions are frequently metastable in their synthesis liquid,[29] it is likely that Al-distribution remains dynamic after prolonged synthesis within a formed zeolite crystal. Specifically in this case, a fraction of the cobalt hosting 2Al-arrangements could disappear in time, striving for a more thermodynamically favored outcome, i.e. Al-isolation. The potential driving force for reshuffling could be repulsive Coulomb interactions of negatively charged $(AlO_4)^-$ centers disfavoring short inter-Al distances, also known as Dempsey's rule.[56] Note that this experimental finding contrasts the recent computational work reflecting that high silica H-SSZ-13 (Si/Al=35) is more stable with certain next nearest neighbors or 'paired' configurations rather than with isolated Al, although the computational conditions differ from our real ones (i.e. here: as-made zeolites, containing OSDA, in equilibrium with their

synthesis liquor).[44, 57] Zeotype materials kept within their synthesis liquor are known to be non-rigid: e.g. Si-islanding is a well-documented phenomenon in silicoaluminophosphates.[58-59] Even more relevant here is the intra-framework T-atom migration proposed by the Hong group upon finding heteroatom reshuffling in gallosilicates at prolonged synthesis times.[60]

The DCC trends at various synthesis temperatures seem to confirm that Al redistribution mechanisms are at play to dynamically change the DCC values. As fully crystalline SSZ-13 is formed within the first three hours, the DCC at high temperatures (≥160°C) is likely affected by post-assembly Al-rearranging processes with high energy barriers. This is also apparent from the larger temporal differences in DCC at 175°C than at 160°C (Figure 2B); and the long term experiment at 180°C that resulted in very low DCC. The long term, thermodynamically driven process towards isolation stands in competition with the short term DCC-favoring mechanisms at lower temperatures (and/or shorter times at high temperature), where a combination of kinetic and thermodynamic factors related to assembly seem to be at the basis of high DCC outcomes (Figure 2).

Tentative analysis aside, the single-parameter analyses of key synthetic factors demonstrates the potential, for the first time, to reliably control DCC over a wide range (Co/Al = 0.01 - 0.35) using the FAU-to-CHA IZC strategy, while syntheses from separate amorphous sources lead to low or no DCC.

3.3. Structure-activity (DCC-MPO) relations in SSZ-13

Earlier, an 'on or off' relation between DCC and MPO productivity was exposed for two SSZ-13 materials from different sources (Table 1, Section 3.1.3.). Here, we aim to establish if a relation or link can be found for a series of IZC based SSZ-13 with large DCC diversity. Despite differences in the nature of the exchange methods, the Co and Fe contents of samples with diverse DCC capacity show positive correlation (Figure S16A). Next, the MeOH productivity of identically exchanged SSZ-13 with different DCC are compared to their Fe-content in figure S16B. A maximum reaction efficiency (MeOH/Fe= 0.41; MeOH/Al=0.067) is obtained in SSZ-13 with medium-high Fe loadings. The variable presence of unreactive Fe_xO_y nanoclusters is likely responsible for the large differences in MeOH/Fe efficiency observed. A more outspoken relation is obtained by plotting the methanol productivity of the Fe-SSZ-13 samples (normalized per Al) against DCC based on Co^{2+} exchange (Figure 3). DCC is thus a better predictor of active site density than Fe/Al ratios. The sample without exchange capacity (Co/Al=0.003) is indeed not able to produce MeOH despite a minor but significant Fe content (Fe/Al=0.05). With a linear fit, the seven SSZ-13 samples with low to medium Co content correlate through the (0,0) coordinate (y=0.24x+0.00, R^2=0.90). The two samples with the highest DCC (Co/Al>0.30; Fe/Al>0.23) are made with very short synthesis times (i.e. 3 and 6 hour for Time-2 and Time-4 respectively) and have lower MeOH/Al productivity than expected. The reasons behind this deviation are not clear. One explanation could be that they contain more faulted regions, causing diffusion limitations for Fe or the reagents. Another explanation could be that the proportionality between Co^{2+} exchange and effective Al-pairs (2Al configuration) is different here (e.g. more Co^{2+} exchange on defect sites or on other 2Al configurations). Including these two samples, the overall linear correlation is less strong, but still significant (blue trend in Figure 3). The maximum productivity obtained for a zeolite with Si/Al_F=30 (IZC-2, Fe-form) is remarkably high (36 µmol MeOH/g zeolite, MeOH/Al=0.067), given that an Al pair in a 6MR is needed for the active site. Calculating back from the methanol formed, this shows that at least 13.5 % of all Al is linked to iron that produces MeOH in this sample. Hence, these data demonstrate that SSZ-13 can be obtained with a higher fraction of Al in pairs than in case of a random distribution of Al (9% of total Al_F in pairs) as predicted by the computational model of Bates et al.[61] Note that the MeOH productivity likely would be higher if steam extraction had been used instead of our liquid extraction, which is known to underestimate MeOH productivity.[27] The direct link between MeOH productivity and Co-exchange validates the latter as a quantitative descriptor for Al arrangements (e.g. in pairs) that allow methane C-H activation on iron-zeolites; here, with SSZ-13 for DCC < 0.3.

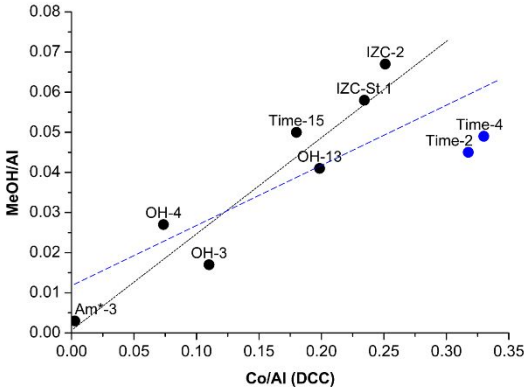

Figure 3. Correlation of MeOH productivity normalized per Al with DCC as determined from Cobalt exchange for a series of SSZ-13 zeolites. Each dot represents one SSZ-13 synthesis and their labels can be traced in SI, Table S4. The seven black dots are fitted by the dotted trend line (y= 0.24 x+ 0.00; R^2=0.90). The blue dashed trend line fits all points (y =0.146x + 0.013; R^2 = 0.65).

3.4. Temporal analysis of FAU-to-CHA synthesis

An in-depth understanding of Al-organization during zeolite crystallization is largely lacking in literature. Factors including the method of gel preparation or dilution are known to lead to different mechanisms for crystal formation and Al-distribution at the molecular level.[42] Here we study a controlled standard interzeolite transformation from FAU-to-CHA in time to gain insight into the factors governing DCC creation (Experimental Section 2.3). A series of identical synthesis were stopped at different times and particle morphology and crystallinity were monitored by ex-situ TEM and PXRD respectively. Furthermore TGA, weighing and elemental analysis were used to estimate Si and Al contents of supernatant and the recovered solid fraction (including remaining FAU, intermediate solid phases and CHA). Evolution of chemical compositions and crystallinity of the solid products of hydrothermal treatment are summarized in Figure 4 (Table S5). Four different stages of the FAU-to-CHA process could be discerned and defined: (I) *incongruent FAU dissolution*, (II) an equilibrium or *induction phase* with steady compositions, (III) the onset of crystallinity with *initial fast assembly* of the bulk of the zeolites, and (IV) *SSZ-13 maturation* with potential internal T-atom rearrangement.

Within the first fifteen minutes of hydrothermal heating in a forced convection oven (surely not reaching 160 °C inside[62]), all long range order is lost (Figure S17). Alkaline dissolution of zeolites consumes OH^-, leading to a rapid decrease in pH of the liquid solution, to pH ~11.7. The pH remains this low until the soluble T-atom species are recrystallized, and most of the mineralizing agent (catalyst) is set free again.[63] To compare, the same composition aged for two hours at room-temperature will keep a pH between 13 and 14. After room temperature aging, FAU reflections remain clearly distinguishable by X-ray diffraction (Figure S18). Clearly, FAU dissolution is thermally activated. At the start of the synthesis the Si to Al ratios of the

liquid phase are very high (Si/Al=180, stage I, 15min) before they drop and stabilize at Si/Al=~70 (induction period, stage II). The faster dissolution of Si than that of Al is typical for zeolites in alkaline media and known as incongruent dissolution.[54]

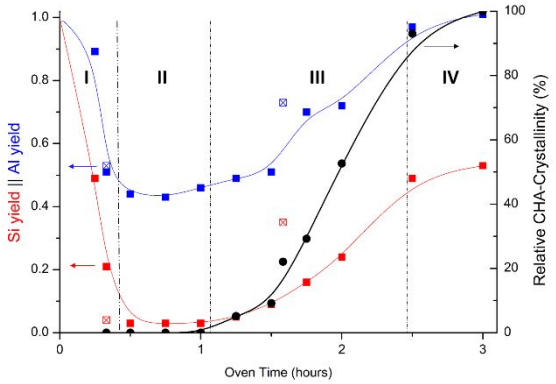

Figure 4. Structural evolution of FAU-to-CHA (1SiO_2: 0.025Al: 0.35$TMAda^+$: 0.35OH^-: 12.5H_2O, 600 rpm, 160 °C). Four different stages are discerned. Si and Al yield refer to the total molar Si and Al recovered in the solid versus the initial input in the synthesis (solid USY). Outliers of yields at 20min and ~1u30 oven time, marked by crossed instead of solid squares, likely result from variability in heating and cooling times (Table S5). Trend lines are added for clarity. Stage IV can be prolonged excessively (e.g. 12 days).

After the initial heating and FAU degradation, the temporal evolution indicates a clearly distinct 'induction period' with little change to the elemental distribution between the solid and liquid phases (Stage II). An equilibrated distribution seems to exist between an amorphous Al-rich solid phase (isolated by centrifugation after brief cooling, result is reproducible) and a Si-rich supernatant. Only a small fraction of T-atom species, i.e. 4% are contained in the Al-rich solids (Si/Al = 3) while the Si-rich supernatant solution (Si/Al = 75-80) contains 97% of Si and 56% of the initial Al (added in form of the FAU parent, table S5). It seems that the remaining solids from FAU breakdown heavily concentrate Al (half of the original content in about 4% of the original solid weight). Constant compositions of the solid phase during induction prior to SSZ-13 crystallization have been observed earlier, in synthesis media using amorphous Si and Al precursors.[64-65] All solid phases from the induction period (30min-1 hour) are amorphous according to X-ray diffraction (Figure S17), and TEM images show the presence of both irregularly shaped aggregates and what seem to have been smooth crystal phases sized 500 nanometers or larger (Figure 5A). These features resemble the FAU crystal habit[66-67] and it is safe to assume they are the remnants of the dissolving starting zeolite, no longer containing long-range order sensitive to X-ray diffraction. TGA profiles of the evolving solids show very limited weight loss during Stage II, while a much larger weight loss was observed during Stage I (Figure S19A). Large weight loss points to combustion of adsorbed (and interacting) species, presumably OSDA ($TMAda^+$) or extensive dehydration (less likely at higher temperatures). It can be assumed that $TMAda^+$ is involved in the process of FAU dissolution during Stage I, while $TMAda^+$ is largely absent on the surface of Al rich solids during Stage II, according to TGA.

Stage II ends at 1h15min with the appearance of PXRD reflections indicating SSZ-13 growth (1h15min, Figure S17). Meanwhile TGA profiles start showing larger weight loss again (Figure S19). They point to combustion of adsorbed (and interacting) OSDA ($TMAda^+$) with the solid for stage III (cfr. Stage I). The fraction of weight loss between 400°C and 600°C gradually rises and stabilizes during Stage IV (Figure S19B). This fraction indicates the burn-off of one encaged or strongly contained $TMAda^+$ per *cha*-cage and qualitatively aligns with CHA-crystallinity. SSZ-13 crystallinity in stage III was also locally seen by local 'fast Fourier transform' (FFT) detection in TEM mode at 1h45min (figure 5B-B2) confirming the presence of cubic SSZ-13 crystals while the bulk of the solid is still amorphous with low overall Si/Al = 9 (Table S5 and Figure 5B-B1). STEM-EDX imaging (1h45min, Figure S20) showed no significant differences in atomic dispersion of Si and Al between the FFT detected CHA and amorphous regions. The gradually rising Si-content of the recovered solids (CHA+amorphous, Figures 4 and 5B) – and of the pure CHA zeolites in a later stage – point to a dynamic supply of T-atoms from the liquid during stage III assembly with nucleation likely initiating in the Al-rich solids. The importance of both the solid and the liquid medium for assembly is further confirmed by split tests and cross experiments as described in Section S6.1. in the Supporting Information. Those experiments reveal the inherent potential to obtain high DCC values for high Si SSZ-13 zeolites made using both the isolated Al-rich solid phases and the liquid supernatants of an IZC synthesis.

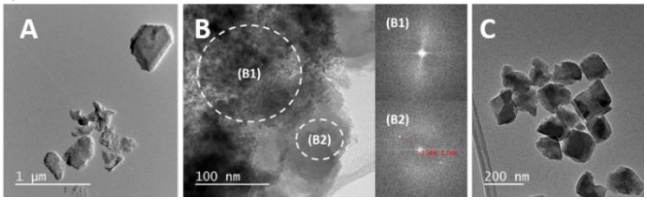

Figure 5. TEM images of solid fractions (1Si: 0.025Al: 0.35$TMAda^+$: 0.35OH^-: 12.5H_2O, 600 rpm, 160 °C). Each image represents different stages of the synthesis process: (A) TEM, after 30min (Stage II); (B) TEM after 1u15min (Stage (III); and (C) TEM after 3 hours of synthesis (Stage IV), this is the Time-2 sample, cfr. Figure S14). Local FFT images of specific regions in B are given.

Stage IV corresponds to prolonged synthesis after a high degree of crystallinity has been reached, i.e. maturation, and witnesses stagnating yields (Figure S15). Si/Al ratios in the zeolite still increase slightly, indicating the consumption of all solid amorphous species. At standard synthesis times of 4 days, but also already after 3h, virtually no Al is found in the liquid phase (Si/Al = ~1000 for 3h) as was also reported by Zones et al. in the early days of IZC synthesis.[63] A lack of freely available Al species after initial fast assembly (Stage III) alters the formation kinetics towards slower assembly with slow yield increase.[68] Changing the kinetics and nature of crystal assembly could allow other factors to play a major role, such as local charge stabilization of $TMAda^+$ species within *cha*-cages with isolated Al. Zeolites harvested right at the end of fast assembly period (late stage III, early stage IV) have the highest DCC values. Stage IV can last as long as the metastable CHA topology persists, but Al reorganization seems to occur (*viz.* Figure 2A and section 3.2.6).

4. DISCUSSION

4.1. Molecular Al-assembly in SSZ-13

Since no evidence for Al zoning[69-70] was encountered in STEM-EDX (Figure S20, S8) a relatively homogenous distribution of Al is assumed (intra-crystalline, *cfr.* a lot of conventional zeolites[71-73]), allowing a focus on Al distribution at the atomic/molecular length scales.

In OSDA-based zeolite syntheses, stabilization of inorganic-organic composite species (IOCSs) is believed to be crucial for phase nucleation (and propagation).[74-76] The quantity and the location of Al inside theses IOCS contributes to optimal CHA

cage stabilization. An ideal framework has 1 TMAda per cage, which needs to be compensated by 1 Al per cage, leads to a theoretical optimal Si/Al ratio of 11. Due to the strong OSDA fit, a much higher compositional variation is possible for CHA crystallization using $TMAda^+$ (SSZ-13).[1] In the case of SSZ-13, energetic (Coulomb) stabilization of localized Al within one cage was initially proposed to explain Al-isolation in the absence of inorganic cations (Na^+).[34] This hypothesis may satisfy for our DCC values encountered in zeolites from amorphous sources (virtually no DCC), but does not explain why high DCC values are encountered in IZC without Na^+. Recent computational work shows that Al has very little energetic preference for specific T-atom location within one *cha* cage, only avoiding locations close to the adamantyl group. Instead, the importance of long-range electrostatic effects between multiple $TMAda^+$–cage complexes is pointed out.[77] This endorses the large variety of Al configurations observed in this study. Some IZC-based recipes also tend towards Al isolation (low DCC for low OSDA/Si, and slow assembly), while most recipes result in high DCC, reflecting strongly diverging mechanisms of Al organization at the molecular level. In fast synthesis, dominated by kinetic control, Al will have less tendency (or time) to assemble to the energetically most favored positions. Crystal habits of the resulting SSZ-13 materials demonstrate differences in supersaturation. Under high supersaturation, crystal growth will evolve much faster, hence affecting the assembly kinetics and growth modes. TEM images (figure 6A) of zeolites made from amorphous sources (Am*-1) reveal large, smooth surfaced cubic crystals. Attached smaller crystals contain the same features typical for 2D layer-by-layer growth (Figure 6, inset). Hence, amorphous synthesis conditions (Am*) show typical crystal habit for a classical growth assembly with relatively low supersaturation. In contrast, IZC based SSZ-13 materials with high DCC are small crystals with irregular surfaces (IZC-2, Figure 6B). Such crystal habit is typically related to conditions of high supersaturation (kinetic roughening). The high Si dissolution (97% in Stage II) and low H_2O/Si (12.5) in this IZC corroborate this.[68]

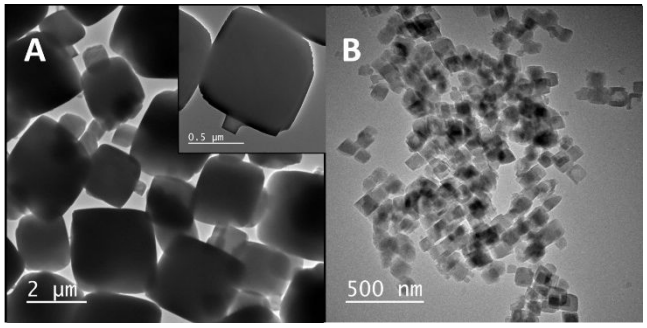

Figure 6. Difference in crystal size and habit of SSZ-13 made from amorphous sources (left, Am*-3) versus IZC synthesis (right, IZC-2) under identical synthetic conditions. The inset of A zooms in on a single crystal.

Conditions favoring a kinetically controlled assembly (away from charge-separating preferences of Al isolation) may influence Al incorporation (and thus DCC) by the manner in which reactive Si and Al species are transferred to the assembling crystal. Zeolites can adopt several growth modes during assembly.[68] While at low supersaturation (*e.g.* at the end of crystallization, Stage IV) zeolites may grow via classical growth – implicating assembly from individual molecules to the growing crystal – they may also experience stages of nonclassical growth with particle attachment preceding disorder-to-order transformation.[64, 68, 78] In the latter case, a multitude of species can serve as putative growth units: nanocrystals (oriented attachment), amorphous particles and so called *nanoparts*[79-80] (oligomers with specific geometries).[68, 81] Little hard evidence is provided in this case, but TGA profiles of initial assembly (Figure S19, Section 3.4) hint towards particle attachment of pre-crystalline regions during initial fast assembly (Stage III). These XRD-amorphous aggregating particles contain adsorbed (organized) OSDA but initially lack CHA long range order.[65] Noteworthy, Muraoka et al. proved that low Si FAU-to-CHA IZC (without OSDA) results in a CHA structure containing specific atomic Al arrangements with lower overall energy than identical recipes from other T-atom sources.[82] Oligomeric growth units may transfer specific molecular Al-configurations originating from the starting FAU to growing CHA crystals by incorporation via atypical growth modes (e.g. pre-crystalline particle attachment). In this way such atomic configurations may be preserved, preventing the formation of thermodynamically more stable Al conformations found in slow synthesis and from classical monomer-by-monomer addition. In case of interzeolite conversion from other zeolites and putative growth units (e.g. MFI pentasils, see 3.2.5), different species and/or different dissolution kinetics (e.g. longer induction) may differently influence Al incorporation and thus DCC.

The correlation between DCC measured by Co-exchange and specific Al arrangements was proven by many authors[38, 42] and supported by MPO tests (3.3). Nonetheless it should be acknowledged that the individual contribution of the following factors on DCC and the ion-exchange process cannot be excluded: the effect of lattice faulting, defect sites, exchange against external surface[83-84] or T-atom flexibility[85] and film diffusion boundaries altering molecular cobalt diffusion. In some of these cases, the nature of exchange may slightly differ, and it cannot be excluded that such factors govern part of the DCC variations observed in this work.

4.2. Tentative hypothesis of Al-organization in IZC

In what follows, a first hypothesis on Al-distribution control (in terms of proximity/pairing) at the nanometer scale is presented for OSDA-containing IZC systems in general, and high Si FAU-to-CHA systems specifically. The hypothesis includes Al-location implications at each stage of interzeolite conversion and relies on observations, literature (section 4.1), general synthetic insights and some conjectures. First, FAU dissolves incongruently upon heating (Stage I, Figure 7). Al-rich solids either remain or form from leached alumina that reattaches to the remaining solid phase via condensation-polymerization.[86] Silica dissolution extends until the surface contains enough Si-O-Al bonds, more resistant to hydroxide attack[54, 87-88] to reach a temporary equilibrium with the liquid phase (evidenced, Figure 4). An Al-enriched solid (Si/Al=3, section 3.4.) is what remains of the FAU. At the end of the 'induction period' (Stage II, Figure 7) nucleation occurs in Al-rich conditions (likely heterogeneously[29, 89]). Next, crystallization installs long range order and causes further condensation. The initial T-atom assembly is a concerted mechanism between remaining Al rich solids and the liquid supernatant (Stage III, Figure 7). The formed crystals are initially low in Si/Al, which gradually increase upon crystallization. The history of T-atom attachment prior to crystallization can partially determine the assembled Al configurations, depending on the growth kinetics. In case of slow growth, with low supersaturation (monomer addition, Figure 7, A) electronically favored Al arrangements can be assembled (e.g. isolated Al in SSZ-13 from amorphous sources and $TMAda^+$). Here, in a case of fast kinetic assembly (*vide supra,* 3.4) and high supersaturation via IZC, alternative growth modes are at the origin of different Al configurations by preventing the drive to achieve lower energy OSDA/T-atom configurations. Fast multispecies assembly, from Al-rich species, i.e. oligomers and amorphous solids (B and C in Figure 7), results in a high, but metastable, divalent cation capacity. The result is a

quickly assembled, small-particle CHA zeolite with rough surfaces and high DCC.

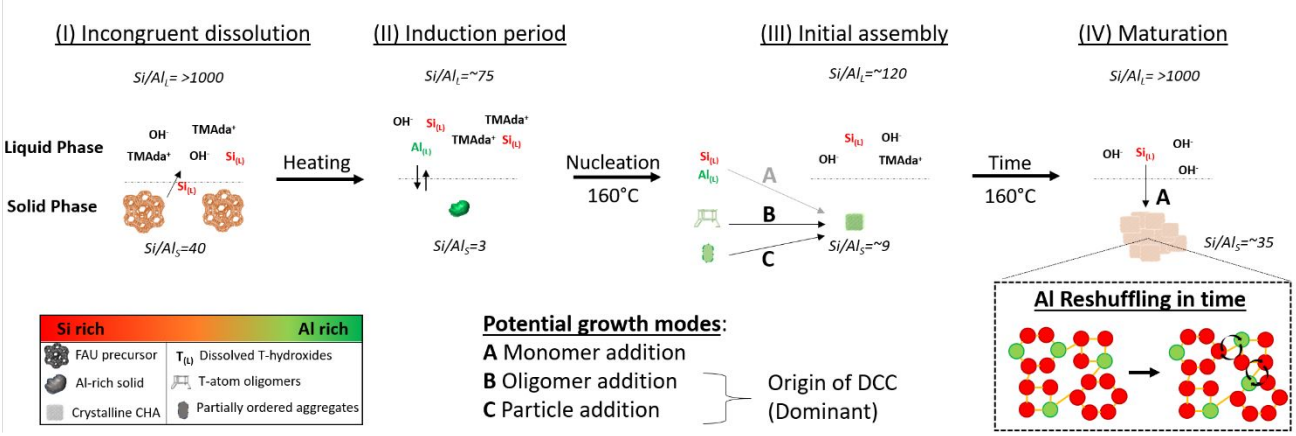

Figure 7. Cartoon of the hypothetic Al-organization mechanism, applied on high Si FAU-to-CHA IZC

The higher tendency of Al for precipitation[86] causes 100% Al incorporation in SSZ-13[63] before fully crystalline materials are obtained, and the crystal growth slows down (Stage IV). During maturation, a lower T-atom content in the remaining liquor lowers supersaturation for further assembly. Additional yield then more likely stems from Si-rich classical growth (mode A, Figure 7). At this point in the hydrothermal synthesis, the obtained crystalline material does not remain rigid, but still strives for higher stability. Prolonged exposure (especially at high temperatures) overcomes the energetic barriers for internal Al rearrangements, implying intraframework Al-migration. The final addition of silica might therefore concur with or facilitate the destruction of a portion of the DCC. Finally, it is interesting to note that certain partial IZC syntheses, i.e. starting from an aluminous FAU and an additional soluble Si-source, resemble the situation in the induction phase obtained from dissolution.[63, 90]

5. CONCLUSIONS

The Fe mononuclear active site and the highly symmetric nature of the CHA framework provides an opportunity to discover unique synthesis-structure-activity relationships in redox-based zeolite catalysis for small molecules. The remarkable methane partial oxidation performance of an Fe-SSZ-13 made via interzeolite conversion with only organic structure directing agents, sparked a closer look into the mechanism of Al-organization in these redox host systems. An exhaustive investigation with single parameter variations and the resulting Al-arrangements probed by Co^{2+}-exchange, discovered remarkable effects demonstrating the importance of often neglected synthesis parameters on the divalent cation capacity of the resulting and calcined zeolite. These parameters include synthesis time, temperature and compositional factors, such as the dilution. Using IZC, control over the DCC of SSZ-13 was established over a wide range (Co/Al = 0.04 - 0.35), yielding reliable synthesis-structure relations. Using DCC as a probe for Al-arrangements capable of hosting Fe^{II}, a structure-activity relation for methanol productivity was demonstrated. Fe^{II}-redox zeolites were made with productivities surpassing the maximum productivity possible with random Al-distributions, confirming their more optimal Al-configuration and the applicability and practicality of the DCC method. Furthermore, DCC evaluation allowed to hypothesize an introduction mechanism of Al in IZC routes. The complex roles of Al in these systems (and most zeolite synthesis in fact) were investigated via a temporal analysis and put into perspective. While the exact mechanism remains to be proven, this work has evidenced that fast synthesis kinetics play a large role in Al-organization, and DCC-rich solids are encountered as a thermodynamic metastable phase in the short term. At a longer term, a decrease in DCC can be encountered as Al-isolation seems to be thermodynamically favored, however a high energetic barrier for reshuffling is likely present. The way in which kinetically fast IZC syntheses can produce the metastable DCC-rich zeolites seems to be linked to the occurrence of atypical modes of assembly (e.g. nonclassical growth, with nanoparts or Al-enriched solids) with an important role for Al-concentration by incongruent dissolution of the starting zeolite. The presented hypothesis paints some guidelines that could be generic for Al-organization in zeolite synthesis. Synthesis media with high Al-enrichment during induction, fast crystallization, atypical assembly modes (Al rich building units avoiding monomer-by-monomer addition) and low maturation times should therefore be ideal candidates as potential hosts for multivalent redox species (high DCC). It is obvious that a lot of IZC synthesis could qualify here although the role of a well-fitting OSDA in this mode of Al-direction cannot be neglected. It is important to highlight the relevance of DCC evaluation when mapping synthesis mechanisms and zeolite dynamics. The unique synthesis-structure-activity relations unearthed here could inspire the search for catalytically relevant Al-ensembles in zeolitic materials of use to a diverse range of transition-metal ion based reactions.

ASSOCIATED CONTENT

Supporting Information

The Supporting Information is available free of charge on the ACS Publications website.

Overview of synthesized samples, XRD diffractograms, nitrogen sorption isotherms, thermogravimetric analysis, SS NMR, additional TEM-images, STEM-EDX mappings of metal containing zeolites, details on divalent cation exchange (DCC) quantification by cobalt exchange, DR-UV−vis−NIR spectra, properties of MPO tested materials, detailed characterization of intermediate phases during FAU-to-CHA conversion and additional synthesis tests using intermediate phases (PDF).

AUTHOR INFORMATION

Corresponding Author

M.D.: michiel.dusselier@kuleuven.be

Notes

The authors declare no competing financial interests.

ACKNOWLEDGMENT

We thank the Research Foundation - Flanders (FWO) for funding (Grants G0A2216N to B.F.S., 12E8617N to M.D, 11D4718N to D.P.). C.V.G. acknowledges the KU Leuven internal funds for a PDM postdoctoral fellowship. S.H. thanks the National Science Foundation (NSF) under Grant Number 9724240 and partially supported by the MRSEC Program of the NSF under Award Number DMR-520565. M.D. acknowledges KU Leuven BOF. J.S. is grateful to Flemish Hercules Foundation (AKUL/13/19). SACHEM is explicitly thanked for providing the TMAdaOH organic structure directing agent.

REFERENCES

1. Dusselier, M.; Davis, M. E., Small-Pore Zeolites: Synthesis and Catalysis. *Chemical Reviews* **2018,** *118* (11), 5265-5329.
2. Moliner, M.; Martínez, C.; Corma, A., Synthesis Strategies for Preparing Useful Small Pore Zeolites and Zeotypes for Gas Separations and Catalysis. *Chemistry of Materials* **2014,** *26* (1), 246-258.
3. Tian, P.; Wei, Y.; Ye, M.; Liu, Z., Methanol to Olefins (MTO): From Fundamentals to Commercialization. *ACS Catalysis* **2015,** *5* (3), 1922-1938.
4. Chowdhury Abhishek, D.; Paioni Alessandra, L.; Houben, K.; Whiting Gareth, T.; Baldus, M.; Weckhuysen Bert, M., Bridging the Gap between the Direct and Hydrocarbon Pool Mechanisms of the Methanol-to-Hydrocarbons Process. *Angewandte Chemie* **2018,** *130* (27), 8227-8231.
5. Yarulina, I.; Chowdhury, A. D.; Meirer, F.; Weckhuysen, B. M.; Gascon, J., Recent trends and fundamental insights in the methanol-to-hydrocarbons process. *Nature Catalysis* **2018,** *1* (6), 398-411.
6. Kwak, J. H.; Tonkyn, R. G.; Kim, D. H.; Szanyi, J.; Peden, C. H. F., Excellent activity and selectivity of Cu-SSZ-13 in the selective catalytic reduction of NOx with NH3. *Journal of Catalysis* **2010,** *275* (2), 187-190.
7. Paolucci, C.; Parekh, A. A.; Khurana, I.; Di Iorio, J. R.; Li, H.; Albarracin Caballero, J. D.; Shih, A. J.; Anggara, T.; Delgass, W. N.; Miller, J. T.; Ribeiro, F. H.; Gounder, R.; Schneider, W. F., Catalysis in a Cage: Condition-Dependent Speciation and Dynamics of Exchanged Cu Cations in SSZ-13 Zeolites. *Journal of the American Chemical Society* **2016,** *138* (18), 6028-6048.
8. Gounder, R.; Moini, A., Automotive NOx abatement using zeolite-based technologies. *Reaction Chemistry & Engineering* **2019,** *4* (6), 966-968.
9. Gao, F.; Peden, C., Recent Progress in Atomic-Level Understanding of Cu/SSZ-13 Selective Catalytic Reduction Catalysts. *Catalysts* **2018,** *8* (4), 140.
10. Lange, J.-P.; Sushkevich, V. L.; Knorpp, A. J.; van Bokhoven, J. A., Methane-to-Methanol via Chemical Looping: Economic Potential and Guidance for Future Research. *Industrial & Engineering Chemistry Research* **2019,** *58* (20), 8674-8680.
11. Kondratenko, E. V.; Peppel, T.; Seeburg, D.; Kondratenko, V. A.; Kalevaru, N.; Martin, A.; Wohlrab, S., Methane conversion into different hydrocarbons or oxygenates: current status and future perspectives in catalyst development and reactor operation. *Catalysis Science & Technology* **2017,** *7* (2), 366-381.
12. Hammond, C.; Conrad, S.; Hermans, I., Oxidative Methane Upgrading. *ChemSusChem* **2012,** *5* (9), 1668-1686.
13. Snyder, B. E. R.; Bols, M. L.; Schoonheydt, R. A.; Sels, B. F.; Solomon, E. I., Iron and Copper Active Sites in Zeolites and Their Correlation to Metalloenzymes. *Chemical Reviews* **2018,** *118* (5), 2718-2768.
14. Narsimhan, K.; Iyoki, K.; Dinh, K.; Román-Leshkov, Y., Catalytic Oxidation of Methane into Methanol over Copper-Exchanged Zeolites with Oxygen at Low Temperature. *ACS Central Science* **2016,** *2* (6), 424-429.
15. Ipek, B.; Lobo, R. F., Catalytic conversion of methane to methanol on Cu-SSZ-13 using N2O as oxidant. *Chemical Communications* **2016,** *52* (91), 13401-13404.
16. Wulfers, M. J.; Teketel, S.; Ipek, B.; Lobo, R. F., Conversion of methane to methanol on copper-containing small-pore zeolites and zeotypes. *Chemical Communications* **2015,** *51* (21), 4447-4450.
17. Pappas, D. K.; Borfecchia, E.; Dyballa, M.; Pankin, I.; Lomachenko, K. A.; Martini, A.; Signorile, M.; Teketel, S.; Arstad, B.; Berlier, G.; Lamberti, C.; Bordiga, S.; Olsbye, U.; Lillerud, K. P.; Svelle, S.; Beato, P., Methane to methanol: structure-activity relationships for Cu-CHA. *Journal of the American Chemical Society* **2017,** *139* (42), 14961-14975.
18. Vanelderen, P.; Snyder, B. E. R.; Tsai, M.-L.; Hadt, R. G.; Vancauwenbergh, J.; Coussens, O.; Schoonheydt, R. A.; Sels, B. F.; Solomon, E. I., Spectroscopic Definition of the Copper Active Sites in Mordenite: Selective Methane Oxidation. *Journal of the American Chemical Society* **2015,** *137* (19), 6383-6392.
19. Ipek, B.; Wulfers, M. J.; Kim, H.; Göltl, F.; Hermans, I.; Smith, J. P.; Booksh, K. S.; Brown, C. M.; Lobo, R. F., Formation of [Cu2O2]2+ and [Cu2O]2+ toward C–H Bond Activation in Cu-SSZ-13 and Cu-SSZ-39. *ACS Catalysis* **2017,** *7* (7), 4291-4303.
20. Kulkarni, A. R.; Zhao, Z.-J.; Siahrostami, S.; Nørskov, J. K.; Studt, F., Monocopper Active Site for Partial Methane Oxidation in Cu-Exchanged 8MR Zeolites. *ACS Catalysis* **2016,** *6* (10), 6531-6536.
21. Grundner, S.; Markovits, M. A. C.; Li, G.; Tromp, M.; Pidko, E. A.; Hensen, E. J. M.; Jentys, A.; Sanchez-Sanchez, M.; Lercher, J. A., Single-site trinuclear copper oxygen clusters in mordenite for selective conversion of methane to methanol. *Nature Communications* **2015,** *6* (1), 7546.
22. Sushkevich, V. L.; Palagin, D.; van Bokhoven, J. A., The Effect of the Active-Site Structure on the Activity of Copper Mordenite in the Aerobic and Anaerobic Conversion of Methane into Methanol. *Angewandte Chemie International Edition* **2018,** *57* (29), 8906-8910.
23. Borfecchia, E.; Lomachenko, K. A.; Giordanino, F.; Falsig, H.; Beato, P.; Soldatov, A. V.; Bordiga, S.; Lamberti, C., Revisiting the nature of Cu sites in the activated Cu-SSZ-13 catalyst for SCR reaction. *Chemical Science* **2015,** *6* (1), 548-563.
24. Göltl, F.; Love, A. M.; Hermans, I., Developing a Thermodynamic Model for the Interactions between Water and Cu in the Zeolite SSZ-13. *The Journal of Physical Chemistry C* **2017,** *121* (11), 6160-6169.
25. Dinh, K. T.; Sullivan, M. M.; Narsimhan, K.; Serna, P.; Meyer, R. J.; Dincă, M.; Román-Leshkov, Y., Continuous Partial Oxidation of Methane to Methanol Catalyzed by Diffusion-Paired Copper Dimers in Copper-Exchanged Zeolites. *Journal of the American Chemical Society* **2019,** *141* (29), 11641-11650.
26. Snyder, B. E. R.; Vanelderen, P.; Bols, M. L.; Hallaert, S. D.; Böttger, L. H.; Ungur, L.; Pierloot, K.; Schoonheydt, R. A.; Sels, B. F.; Solomon, E. I., The active site of low-temperature methane hydroxylation in iron-containing zeolites. *Nature* **2016,** *536* (7616), 317-321.
27. Bols, M. L.; Hallaert, S. D.; Snyder, B. E. R.; Devos, J.; Plessers, D.; Rhoda, H. M.; Dusselier, M.; Schoonheydt, R. A.; Pierloot, K.; Solomon, E. I.; Sels, B. F., Spectroscopic Identification of the α-Fe/α-O Active Site in Fe-CHA Zeolite for the Low-Temperature Activation of the Methane C–H Bond. *Journal of the American Chemical Society* **2018,** *140* (38), 12021-12032.
28. Hallaert, S. D.; Bols, M. L.; Vanelderen, P.; Schoonheydt, R. A.; Sels, B. F.; Pierloot, K., Identification of α-Fe in High-Silica Zeolites on the Basis of ab Initio Electronic Structure Calculations. *Inorganic Chemistry* **2017,** *56* (17), 10681-10690.

29. Cundy, C. S.; Cox, P. A., The hydrothermal synthesis of zeolites: Precursors, intermediates and reaction mechanism. *Microporous and Mesoporous Materials* **2005,** *82* (1–2), 1-78.
30. Anthony, J. L.; Davis, M. E., Assembly of Zeolites and Crystalline Molecular Sieves. In *Self-Organized Nanoscale Materials*, Adachi, M.; Lockwood, D. J., Eds. Springer New York: New York, NY, 2006; pp 159-185.
31. Pinar, A. B.; Gómez-Hortigüela, L.; McCusker, L. B.; Pérez-Pariente, J., Controlling the Aluminum Distribution in the Zeolite Ferrierite via the Organic Structure Directing Agent. *Chemistry of Materials* **2013,** *25* (18), 3654-3661.
32. Yokoi, T.; Mochizuki, H.; Namba, S.; Kondo, J. N.; Tatsumi, T., Control of the Al Distribution in the Framework of ZSM-5 Zeolite and Its Evaluation by Solid-State NMR Technique and Catalytic Properties. *The Journal of Physical Chemistry C* **2015,** *119* (27), 15303-15315.
33. Román-Leshkov, Y.; Moliner, M.; Davis, M. E., Impact of Controlling the Site Distribution of Al Atoms on Catalytic Properties in Ferrierite-Type Zeolites. *The Journal of Physical Chemistry C* **2011,** *115* (4), 1096-1102.
34. Di Iorio, J. R.; Gounder, R., Controlling the Isolation and Pairing of Aluminum in Chabazite Zeolites Using Mixtures of Organic and Inorganic Structure-Directing Agents. *Chemistry of Materials* **2016,** *28* (7), 2236-2247.
35. Pashkova, V.; Sklenak, S.; Klein, P.; Urbanova, M.; Dědeček, J., Location of Framework Al Atoms in the Channels of ZSM-5: Effect of the (Hydrothermal) Synthesis. *Chemistry – A European Journal* **2016,** *22* (12), 3937-3941.
36. Muraoka, K.; Chaikittisilp, W.; Yanaba, Y.; Yoshikawa, T.; Okubo, T., Directing Aluminum Atoms into Energetically Favorable Tetrahedral Sites in a Zeolite Framework by Using Organic Structure-Directing Agents. *Angewandte Chemie International Edition* **2018,** *57* (14), 3742-3746.
37. Knott, B. C.; Nimlos, C. T.; Robichaud, D. J.; Nimlos, M. R.; Kim, S.; Gounder, R., Consideration of the Aluminum Distribution in Zeolites in Theoretical and Experimental Catalysis Research. *ACS Catalysis* **2017,** *8* (2), 770-784.
38. Dědeček, J.; Sobalík, Z.; Wichterlová, B., Siting and Distribution of Framework Aluminium Atoms in Silicon-Rich Zeolites and Impact on Catalysis. *Catalysis Reviews* **2012,** *54* (2), 135-223.
39. Biligetu, T.; Wang, Y.; Nishitoba, T.; Otomo, R.; Park, S.; Mochizuki, H.; Kondo, J. N.; Tatsumi, T.; Yokoi, T., Al distribution and catalytic performance of ZSM-5 zeolites synthesized with various alcohols. *Journal of Catalysis* **2017,** *353*, 1-10.
40. Di Iorio, J. R.; Nimlos, C. T.; Gounder, R., Introducing Catalytic Diversity into Single-Site Chabazite Zeolites of Fixed Composition via Synthetic Control of Active Site Proximity. *ACS Catalysis* **2017,** *7* (10), 6663-6674.
41. Liang, T. Y.; Chen, J. L.; Qin, Z. F.; Li, J. F.; Wang, P. F.; Wang, S.; Wang, G. F.; Dong, M.; Fan, W. B.; Wang, J. G., Conversion of Methanol to Olefins over H-ZSM-5 Zeolite: Reaction Pathway Is Related to the Framework Aluminum Siting. *Acs Catalysis* **2016,** *6* (11), 7311-7325.
42. Dědeček, J.; Tabor, E.; Sklenak, S., Tuning the Aluminum Distribution in Zeolites to Increase their Performance in Acid-Catalyzed Reactions. *ChemSusChem* **2019,** *12* (3), 556-576.
43. Mlekodaj, K.; Dedecek, J.; Pashkova, V.; Tabor, E.; Klein, P.; Urbanova, M.; Karcz, R.; Sazama, P.; Whittleton, S. R.; Thomas, H. M.; Fishchuk, A. V.; Sklenak, S., Al Organization in the SSZ-13 Zeolite. Al Distribution and Extraframework Sites of Divalent Cations. *The Journal of Physical Chemistry C* **2019,** *123* (13), 7968-7987.
44. Li, S.; Li, H.; Gounder, R.; Debellis, A.; Müller, I. B.; Prasad, S.; Moini, A.; Schneider, W. F., First-Principles Comparison of Proton and Divalent Copper Cation Exchange Energy Landscapes in SSZ-13 Zeolite. *The Journal of Physical Chemistry C* **2018,** *122* (41), 23564-23573.
45. Fickel, D. W.; Lobo, R. F., Copper Coordination in Cu-SSZ-13 and Cu-SSZ-16 Investigated by Variable-Temperature XRD. *The Journal of Physical Chemistry C* **2010,** *114* (3), 1633-1640.
46. Janda, A.; Bell, A. T., Effects of Si/Al Ratio on the Distribution of Framework Al and on the Rates of Alkane Monomolecular Cracking and Dehydrogenation in H-MFI. *Journal of the American Chemical Society* **2013,** *135* (51), 19193-19207.
47. Wang, S.; Wang, P. F.; Qin, Z. F.; Chen, Y. Y.; Dong, M.; Li, J. F.; Zhang, K.; Liu, P.; Wang, J. G.; Fang, W. B., Relation of Catalytic Performance to the Aluminum Siting of Acidic Zeolites in the Conversion of Methanol to Olefins, Viewed via a Comparison between ZSM-5 and ZSM-11. *Acs Catalysis* **2018,** *8* (6), 5485-5505.
48. Kim, S.; Park, G.; Woo, M. H.; Kwak, G.; Kim, S. K., Control of Hierarchical Structure and Framework-Al Distribution of ZSM-5 via Adjusting Crystallization Temperature and Their Effects on Methanol Conversion. *ACS Catalysis* **2019,** *9* (4), 2880-2892.
49. H. van Bekkum; Flanigen, E. M.; Jacobs, P. A.; Jansen, J. C., *Introduction to Zeolite Science and Practice, 2nd edition*. Elsevier, Amsterdam: 2001.
50. Nishitoba, T.; Yoshida, N.; Kondo, J. N.; Yokoi, T., Control of Al Distribution in the CHA-Type Aluminosilicate Zeolites and Its Impact on the Hydrothermal Stability and Catalytic Properties. *Industrial & Engineering Chemistry Research* **2018,** *57* (11), 3914-3922.
51. Kovarik, L.; Washton, N. M.; Kukkadapu, R.; Devaraj, A.; Wang, A.; Wang, Y.; Szanyi, J.; Peden, C. H. F.; Gao, F., Transformation of Active Sites in Fe/SSZ-13 SCR Catalysts during Hydrothermal Aging: A Spectroscopic, Microscopic, and Kinetics Study. *ACS Catalysis* **2017,** *7* (4), 2458-2470.
52. Tang, L.; Haw, K.-G.; Zhang, Y.; Fang, Q.; Qiu, S.; Valtchev, V., Fast and efficient synthesis of SSZ-13 by interzeolite conversion of Zeolite Beta and Zeolite L. *Microporous and Mesoporous Materials* **2019,** *280*, 306-314.
53. Xu, H.; Chen, W.; Wu, Q.; Lei, C.; Zhang, J.; Han, S.; Zhang, L.; Zhu, Q.; Meng, X.; Dai, D.; Maurer, S.; Parvulescu, A.-N.; Müller, U.; Zhang, W.; Yokoi, T.; Bao, X.; Marler, B.; De Vos, D. E.; Kolb, U.; Zheng, A.; Xiao, F.-S., Transformation synthesis of aluminosilicate SSZ-39 zeolite from ZSM-5 and beta zeolite. *Journal of Materials Chemistry A* **2019,** *7* (9), 4420-4425.
54. Čižmek, A.; Subotić, B.; Aiello, R.; Crea, F.; Nastro, A.; Tuoto, C., Dissolution of high-silica zeolites in alkaline solutions I. Dissolution of silicalite-1 and ZSM-5 with different aluminum content. *Microporous Materials* **1995,** *4* (2), 159-168.
55. Qin, W.; Zhou, Y.; Rimer, J. D., Deleterious effects of non-framework Al species on the catalytic performance of ZSM-5 crystals synthesized at low temperature. *Reaction Chemistry & Engineering* **2019,** *4* (11), 1957-1968.
56. Dempsey, E.; Kuehl, G. H.; Olson, D. H., Variation of the lattice parameter with aluminum content in synthetic sodium faujasites. Evidence for ordering of the framework ions. *The Journal of Physical Chemistry* **1969,** *73* (2), 387-390.
57. Fletcher, R. E.; Ling, S.; Slater, B., Violations of Löwenstein's rule in zeolites. *Chemical Science* **2017,** *8* (11), 7483-7491.
58. Gómez-Hortigüela, L.; Márquez-Álvarez, C.; Grande-Casas, M.; García, R.; Pérez-Pariente, J., Tailoring the acid strength of microporous silicoaluminophosphates through the use of mixtures of templates: Control of the silicon incorporation mechanism. *Microporous and Mesoporous Materials* **2009,** *121* (1), 129-137.
59. Buchholz, A.; Wang, W.; Xu, M.; Arnold, A.; Hunger, M., Thermal stability and dehydroxylation of Brønsted acid sites in silicoaluminophosphates H-SAPO-11, H-SAPO-18, H-SAPO-31, and H-SAPO-34 investigated by multi-nuclear solid-state NMR spectroscopy. *Microporous and Mesoporous Materials* **2002,** *56* (3), 267-278.
60. Shin, J.; Ahn, N. H.; Camblor, M. A.; Cho, S. J.; Hong, S. B., Intraframework Migration of Tetrahedral Atoms in a Zeolite. *Angewandte Chemie International Edition* **2014,** *53* (34), 8949-8952.
61. Bates, S. A.; Verma, A. A.; Paolucci, C.; Parekh, A. A.; Anggara, T.; Yezerets, A.; Schneider, W. F.; Miller, J. T.; Delgass, W. N.; Ribeiro, F. H., Identification of the active Cu site in standard selective catalytic reduction with ammonia on Cu-SSZ-13. *Journal of Catalysis* **2014,** *312* (0), 87-97.
62. Vandermeersch, T.; Van Assche, T. R. C.; Denayer, J. F. M.; De Malsche, W., A continuous flow reactor setup as a tool for rapid synthesis of micron sized NaA zeolite. *Microporous and Mesoporous Materials* **2016,** *226*, 133-139.
63. Zones, S. I., Conversion of faujasites to high-silica chabazite SSZ-13 in the presence of N,N,N-trimethyl-1-adamantammonium iodide. *Journal of the Chemical Society, Faraday Transactions* **1991,** *87* (22), 3709-3716.
64. Kumar, M.; Luo, H.; Román-Leshkov, Y.; Rimer, J. D., SSZ-13 Crystallization by Particle Attachment and Deterministic

Pathways to Crystal Size Control. *Journal of the American Chemical Society* **2015,** *137* (40), 13007-13017.
65. Umeda, T.; Yamada, H.; Ohara, K.; Yoshida, K.; Sasaki, Y.; Takano, M.; Inagaki, S.; Kubota, Y.; Takewaki, T.; Okubo, T.; Wakihara, T., Comparative Study on the Different Interaction Pathways between Amorphous Aluminosilicate Species and Organic Structure-Directing Agents Yielding Different Zeolite Phases. *The Journal of Physical Chemistry C* **2017,** *121* (43), 24324-24334.
66. Yashiki, A.; Honda, K.; Fujimoto, A.; Shibata, S.; Ide, Y.; Sadakane, M.; Sano, T., Hydrothermal conversion of FAU zeolite into LEV zeolite in the presence of non-calcined seed crystals. *Journal of Crystal Growth* **2011,** *325* (1), 96-100.
67. Boruntea, C.-R.; Lundegaard, L. F.; Corma, A.; Vennestrøm, P. N. R., Crystallization of AEI and AFX zeolites through zeolite-to-zeolite transformations. *Microporous and Mesoporous Materials* **2019,** *278*, 105-114.
68. Kumar, M.; Choudhary, M. K.; Rimer, J. D., Transient modes of zeolite surface growth from 3D gel-like islands to 2D single layers. *Nature Communications* **2018,** *9* (1), 2129.
69. Danilina, N.; Krumeich, F.; Castelanelli, S. A.; van Bokhoven, J. A., Where Are the Active Sites in Zeolites? Origin of Aluminum Zoning in ZSM-5. *The Journal of Physical Chemistry C* **2010,** *114* (14), 6640-6645.
70. Oleksiak, M. D.; Soltis, J. A.; Conato, M. T.; Penn, R. L.; Rimer, J. D., Nucleation of FAU and LTA Zeolites from Heterogeneous Aluminosilicate Precursors. *Chemistry of Materials* **2016,** *28* (14), 4906-4916.
71. Perea, D. E.; Arslan, I.; Liu, J.; Ristanović, Z.; Kovarik, L.; Arey, B. W.; Lercher, J. A.; Bare, S. R.; Weckhuysen, B. M., Determining the location and nearest neighbours of aluminium in zeolites with atom probe tomography. *Nature Communications* **2015,** *6*, 7589.
72. Schmidt, J. E.; Oord, R.; Guo, W.; Poplawsky, J. D.; Weckhuysen, B. M., Nanoscale tomography reveals the deactivation of automotive copper-exchanged zeolite catalysts. *Nature Communications* **2017,** *8* (1), 1666.
73. Lemishko, T.; Jiménez-Ruiz, M.; Rey, F.; Valencia, S.; Blasco, T.; Vidal Moya, A.; Sastre, G., Inelastic Neutron Scattering Study of the Aluminum and Brønsted Site Location in Aluminosilicate LTA Zeolites. *The Journal of Physical Chemistry C* **2018,** *122* (21), 11450-11454.
74. Burkett, S. L.; Davis, M. E., Mechanism of Structure Direction in the Synthesis of Si-ZSM-5: An Investigation by Intermolecular 1H-29Si CP MAS NMR. *The Journal of Physical Chemistry* **1994,** *98* (17), 4647-4653.
75. Ren, N.; Subotić, B.; Bronić, J.; Tang, Y.; Dutour Sikirić, M.; Mišić, T.; Svetličić, V.; Bosnar, S.; Antonić Jelić, T., Unusual Pathway of Crystallization of Zeolite ZSM-5 in a Heterogeneous System: Phenomenology and Starting Considerations. *Chemistry of Materials* **2012,** *24* (10), 1726-1737.
76. Ren, N.; Bosnar, S.; Bronić, J.; Dutour Sikirić, M.; Mišić, T.; Svetličić, V.; Mao, J.-J.; Antonić Jelić, T.; Hadžija, M.; Subotić, B., Role of Subcolloidal (Nanosized) Precursor Species in the Early Stage of the Crystallization of Zeolites in Heterogeneous Systems. *Langmuir* **2014,** *30* (28), 8570-8579.
77. Li, S.; Gounder, R.; DeBellis, A. D.; Muller, I. B.; Prasad, S.; Moini, A.; Schneider, W. F., Influence of N,N,N-trimethyl-1-adamantyl Ammonium Structure Directing Agent on Al Substitution in SSZ-13 Zeolite. *The Journal of Physical Chemistry C* **2019**.
78. Lupulescu, A. I.; Rimer, J. D., In Situ Imaging of Silicalite-1 Surface Growth Reveals the Mechanism of Crystallization. *Science* **2014,** *344* (6185), 729-732.
79. Li, C.; Moliner, M.; Corma, A., Building Zeolites from Precrystallized Units: Nanoscale Architecture. *Angewandte Chemie International Edition* **2018,** *57* (47), 15330-15353.
80. Honda, K.; Itakura, M.; Matsuura, Y.; Onda, A.; Ide, Y.; Sadakane, M.; Sano, T., Role of structural similarity between starting zeolite and product zeolite in the interzeolite conversion process. *Journal of Nanoscience and Nanotechnology* **2013,** *13*, 3020-3026.
81. De Yoreo, J. J.; Gilbert, P. U. P. A.; Sommerdijk, N. A. J. M.; Penn, R. L.; Whitelam, S.; Joester, D.; Zhang, H.; Rimer, J. D.; Navrotsky, A.; Banfield, J. F.; Wallace, A. F.; Michel, F. M.; Meldrum, F. C.; Cölfen, H.; Dove, P. M., Crystallization by particle attachment in synthetic, biogenic, and geologic environments. *Science* **2015,** *349* (6247), aaa6760.
82. Muraoka, K.; Sada, Y.; Shimojima, A.; Chaikittisilp, W.; Okubo, T., Tracking the rearrangement of atomic configurations during the conversion of FAU zeolite to CHA zeolite. *Chemical Science* **2019,** *10* (37), 8533-8540.
83. Montanari, T.; Bevilacqua, M.; Resini, C.; Busca, G., UV−Vis and FT-IR Study of the Nature and Location of the Active Sites of Partially Exchanged Co−H Zeolites. *The Journal of Physical Chemistry B* **2004,** *108* (7), 2120-2127.
84. Essid, S.; Ayari, F.; Bulánek, R.; Vaculík, J.; Asedegbega–Nieto, E.; Mhamdi, M.; Delahay, G.; Ghorbel, A., Solid–state ion exchange of CoCl2·6H2O into NH4+–Beta zeolite: Pathway analysis. *Microporous and Mesoporous Materials* **2018,** *264*, 218-229.
85. Shin, J.; Bhange, D. S.; Camblor, M. A.; Lee, Y.; Kim, W. J.; Nam, I.-S.; Hong, S. B., Tetrahedral Atom Ordering in a Zeolite Framework: A Key Factor Affecting Its Physicochemical Properties. *Journal of the American Chemical Society* **2011,** *133* (27), 10587-10598.
86. Harvey, G.; Dent Glasser, L. S., Structure and Properties of Aluminosilicate Solutions and Gels. in *Zeolite Synthesis*, Eds. Robson H.E. and Occelli M.L. American Chemical Society, Washington, D.C., USA: 1989; Vol. 398, pp 49-65.
87. Dessau, R. M.; Valyocsik, E. W.; Goeke, N. H., Aluminum zoning in ZSM-5 as revealed by selective silica removal. *Zeolites* **1992,** *12* (7), 776-779.
88. Lechert, H.; Kacirek, H., Investigations on the crystallization of X-type zeolites. *Zeolites* **1991,** *11* (7), 720-728.
89. Li, R.; Chawla, A.; Linares, N.; Sutjianto, J. G.; Chapman, K. W.; Martínez, J. G.; Rimer, J. D., Diverse Physical States of Amorphous Precursors in Zeolite Synthesis. *Industrial & Engineering Chemistry Research* **2018,** *57* (25), 8460-8471.
90. Dusselier, M.; Schmidt, J. E.; Moulton, R.; Haymore, B.; Hellums, M.; Davis, M. E., Influence of Organic Structure Directing Agent Isomer Distribution on the Synthesis of SSZ-39. *Chemistry of Materials* **2015,** *27* (7), 2695-2702.

Table of Contents (TOC) graphic: